A Versatile Route for the Synthesis of Single Crystalline Oxide Nanorods

Chen, Zhenguo; Pei, F.; Pei, Y.T.; Hosson, J.Th.M. De

Published in:
Crystal Growth & Design

DOI:
10.1021/cg901558n

Publication date:
2010

DOI: 10.1021/cg901558n

CRYSTAL GROWTH & DESIGN Article

2010, Vol. 10
2585–2590

A Versatile Route for the Synthesis of Single Crystalline Oxide Nanorods: Growth Behavior and Field Emission Characteristics

Z. G. Chen, F. Pei, Y. T. Pei,* and J. Th. M. De Hosson*

Department of Applied Physics, Materials Innovation Institute M2i, University of Groningen, Nijenborgh 4, 9747 AG, Groningen, The Netherlands

Received December 11, 2009; Revised Manuscript Received March 19, 2010

ABSTRACT: The exploration of novel synthetic methodologies that control both size and shape of functional nanostructures opens new avenues for the functional application of nanomaterials. Here we report a new and versatile approach to synthesize single crystalline oxides nanorods: thermal conversion from amorphous oxides nanoparticle precursor ($RuO_2 \cdot xH_2O$ nanoparticle precursor was used as a model system). The shape and size of RuO_2 nanorods can be well controlled by varying the heat-treatment conditions in ambient air. The mechanisms involved are the following: thermal dissociation−crystallization process, including surface diffusion, heterogeneous nucleation, and subsequent anisotropic growth into nanorods on silicon substrate governed by the Wulff construction rule. Additional experiments show also the successful conversion of $IrO_2 \cdot xH_2O$ nanoparticle precursors into nanorods of IrO_2. Therefore, this novel approach based on the thermal conversion of amorphous nanoparticles precursor into single crystalline nanorods points at a general route for the synthesis of one-dimensional oxide nanomaterials. We have tested the functional properties of the nanorods regarding field emission and the results indicate that RuO_2 nanorods can act as excellent field emitters.

1. Introduction

One-dimensional (1D) nanostructures − nanorods (NRs), nanowires (NWs), nanobelts, and nanotubes−bear fascinating applications as potential functional building blocks for a new generation of devices such as sensors, electrodes, and interconnects.[1−3] Numerous studies have been devoted to the synthesis of 1D nanostructures, among which vapor−liquid−solid or vapor−solid processes, templating, capping reagent, or surfactant induced anisotropy are the most widely adopted strategies for achieving size and shape control.[4−6] In general, amorphous nanoparticles (NPs) of spherical shape can be readily produced at a high throughput using a wet chemical approach. Accordingly, self-assembly of NPs has been recently put forward for the synthesis of 1D nanostructures.[7−9]

In particular, ruthenium oxide (RuO_2) exhibits an excellent chemical and thermal stability, and remarkable electric conductivity and optical properties. RuO_2 has been widely used in the oxidation of CO, hydrogenation, direct methanol fuel cells,[10] high energy density capacitors, and corrosion resistant electrodes.[11] For the fabrication of RuO_2 NRs/NWs arrays, the current synthesis methods include chemical vapor deposition (CVD)[12] and radio frequency magnetron sputtering (RFMS) deposition.[13]

In this paper, we report a new and versatile approach to synthesize single crystalline nanorods of oxide materials, and in particular we show results of various oxides, such as RuO_2 and IrO_2. The method is based on the thermal conversion of amorphous $RuO_2 \cdot xH_2O$ nanoparticles and consists of two steps: synthesis of amorphous $RuO_2 \cdot xH_2O$ nanoparticles precursor and heat treatment of the precursor in air. Attractive features of this method comprise simplicity, low cost, high throughput, and generality. As we will show, the method is applicable over a wide temperature range for the thermal conversion, and the morphologies of the nanorods can be controlled to a great extent.

2. Experimental Section

To synthesize $RuO_2 \cdot xH_2O$ amorphous nanoparticles precursor, $RuCl_3 \cdot xH_2O$ powder was dissolved in deionized water. Because of the hydrolysis of $RuCl_3 \cdot xH_2O$, the pH value of the solution dropped to about 2.2. Then stoichiometric amounts of sodium hydroxide solution was added drop by drop into the solution. $RuO_2 \cdot xH_2O$ precipitation occurred to neutralize the added hydroxide anion while the adding speed of NaOH solution was manipulated in order to ensure the precipitation was done around pH 4.0. After half an hour, the as-formed $RuO_2 \cdot xH_2O$ amorphous precipitates were separated from the reaction system and rinsed several times by deionized water. The $RuO_2 \cdot xH_2O$ NPs are amorphous, confirmed by X-ray diffraction (XRD) and selected area electron diffraction (SAED) in TEM (not shown). Thereafter, the $RuO_2 \cdot xH_2O$ nanoparticles redispersed in water were spread on p-type silicon-(100) wafer substrates. The cleaning of the wafers follows the procedure described in ref 14. First, it is cleaned by the Radio Corporation of America (RCA) procedure and followed by etching in HF/methanol solution to obtain a clean ordered (1×1)Si(100) surface.[14]

The precursor nanoparticles and converted nanorods were characterized with X-ray diffraction (XRD, Bruker-AXS D8), high-resolution scanning electron microscopy (SEM, Philips XL-30s FEG) attached with energy dispersive X-ray spectroscopy (EDS, EDAX), transmission electron microscopy (TEM, JEOL 2010F operating at 200 kV), and field emission testing in a focused ion beam (FIB)/FEG SEM microscope (Tescan Lyra, Czech Republic). To manipulate the tungsten tip of the 50 nm radius for in situ field emission test, a SmarAct 4D nanomanipulation system of sub-nanometer resolution (SmarAct GmbH, Germany) was installed inside the Lyra FIB/SEM microscope. A programmable DC 0−30 V power source (Delta Electronika, ES030-10), a Keithley 2182A nanovoltmeter, and a Keithley 6485 picoammeter were used for the field emission test.

3. Results and Discussion

The $RuO_2 \cdot xH_2O$ precursor nanoparticles redispersed in water were spread on cleaned p-type silicon-(100) wafer substrates. Dispersion of the amorphous $RuO_2 \cdot xH_2O$ NPs precursors

*To whom correspondence should be addressed. E-mail: y.pei@rug.nl (Y.T.P.), j.t.m.de.hosson@rug.nl (J.T.M.dH.).

Published on Web 04/22/2010

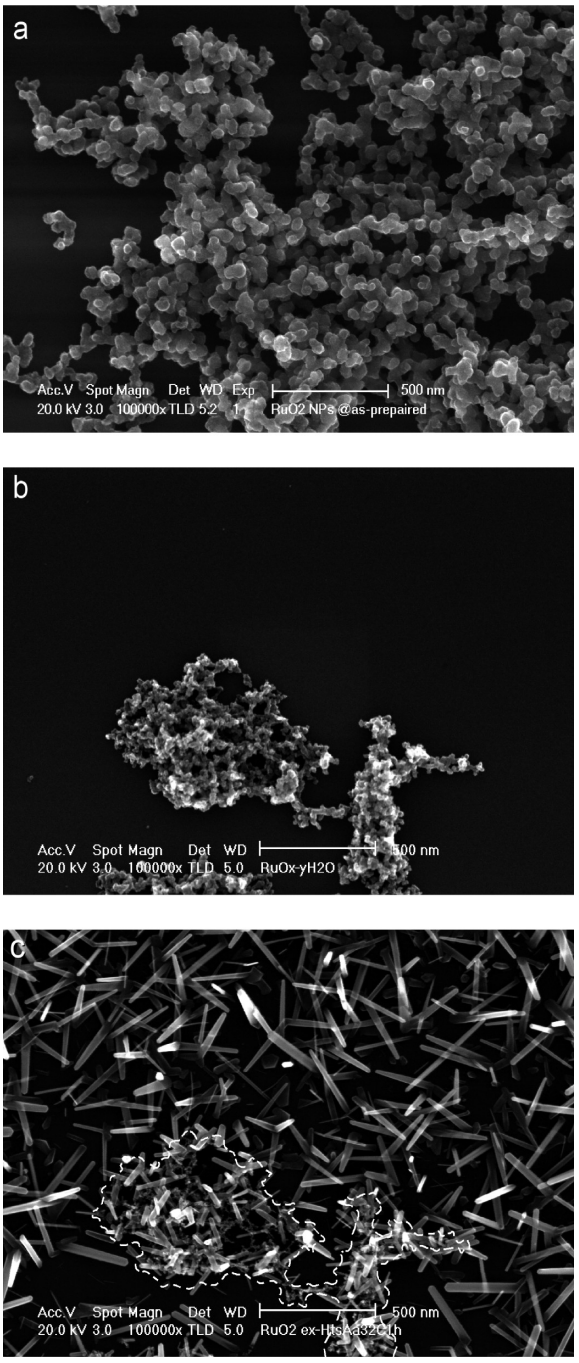

Figure 1. (a) As-prepared $RuO_2 \cdot xH_2O$ NPs precursor layer on Si-wafer, (b) SEM micrograph of $RuO_2 \cdot xH_2O$ NPs precursor cluster before heat treatment, and (c) ex situ SEM micrograph of RuO_2 NRs converted at 320 °C for 1 h. The dashed line indicates the original border of the NPs precursor cluster shown in (b).

formed a discontinuous island-like thin film on the silicon wafer, with a coverage ratio of about 50%. The thickness of the film was estimated at 100−200 nm, as shown in Figure 1a. SEM observations reveal the NPs of spherical morphology with a diameter of around 40 nm.

Heat treatment of the precursor NPs was done in a resistance furnace at different temperatures (280−480 °C) in ambient atmosphere. After 1 h heating, the amorphous $RuO_2 \cdot xH_2O$ NPs were converted into RuO_2 NRs, as shown in Figure 1c for the specimen heat treated at 320 °C. The NRs randomly grow up on the Si-wafer substrate, without any preferred orientation, suggesting nonepitaxial growth. Nevertheless, the NRs are quite uniform in length and diameter and may have few branches grown from one root. Since most of the NRs incline to the substrate, their average length may be estimated from the lengths projected on two SEM micrographs of different tilt angles and the average diameter is measured at the middle length of the obelisk-shaped NRs.

The $RuO_2 \cdot xH_2O$ NPs precursor contains free water and crystal water. During heating, free water evaporates first at lower temperatures up to 100 °C. In contrast, the crystal water decomposes at a higher temperature of around 320 °C, according to the result of differential scanning calorimetry.[10] Ruthenium oxide has a melting point of 1200 °C, and melting should be characterized as an endothermal peak in differential scanning calorimetry (DSC) curve. As confirmed by the DSC result, however, around 320 °C there is an exothermal peak widened between 280 and 360 °C.[10] Thereby, the conversion of amorphous nanoparticles to crystalline nanorods is considered as a solid dissociation−crystallization process boosted by surface diffusion over the substrate, as supported by the ex situ SEM observations shown in Figure 1b,c. During heating, the $RuO_2 \cdot xH_2O$ precursor NPs tend to diffuse away, nucleate, and grow on the surrounding area of Si(100) wafer, instead of locally nucleating on the precursor NPs themselves. This is indicated by the residual precursor NPs marked in the dashed line (Figure 1c). To favor the dissociation−crystallization process, the activation energy for diffusion of the $RuO_2 \cdot xH_2O$ precursors must be lower than the crystallization energy. In addition, heterogeneous nucleation on the Si substrate has to be favorable in the surrounding area.

To study the kinetics of this thermal conversion process, the heat treatments were carried out at different temperatures from 280 °C up to 480 °C for 1 h, and the results are shown in Figure 2 and Table 1. By heating at 280 °C, only few NRs form with an average diameter of 28.9 nm and length of 347 nm. Interestingly, most NRs exhibit a needle shape with a sharp top end of a few nanometers in diameter while the bottom-end has an approximate diameter of 40 nm. After increasing the temperature of heat treatment to 300 °C, a large amount of NRs form and have a more uniform diameter along the axial direction with an average size of 16.5 nm and an average length of 118 nm. The heat treatment at 320 °C yields similar NRs with an average diameter of 46.3 nm and an average length of 499 nm but having the highest aspect ratio of ∼11 among all the NRs specimens. At even higher temperatures, the morphology of the NRs does not change significantly, except the quick increase in the length and diameter and better visible surface facets. However, the amount of NRs per unit area decreases considerably when the temperature is above 300 °C, as is shown in Figure 3. This is mainly attributed to the enhanced growth rate of RuO_2 NRs at higher temperatures and possibly due to Ostwald ripening as diffusion takes over nucleation. Therefore, the growth behavior of RuO_2 NRs over the temperature range of heat treatment may be split into two different regimes: nucleation control below 300 °C and growth control above 300 °C.

EDS analyses were performed to examine the purity of both the precursor and the converted NRs. As shown in Figure 4a, only elements of Si, Ru, O, and C are detected, indicating no impurity except carbon that always presents in an EDS spectrum due to the contamination of the vacuum system. The insets show the detail of the Ru L peak at 2.558 keV and K peak at 19.252 keV, respectively. Figure 4b presents the XRD pattern of RuO_2 NRs grown at 360 °C for 1 h on Si(100)

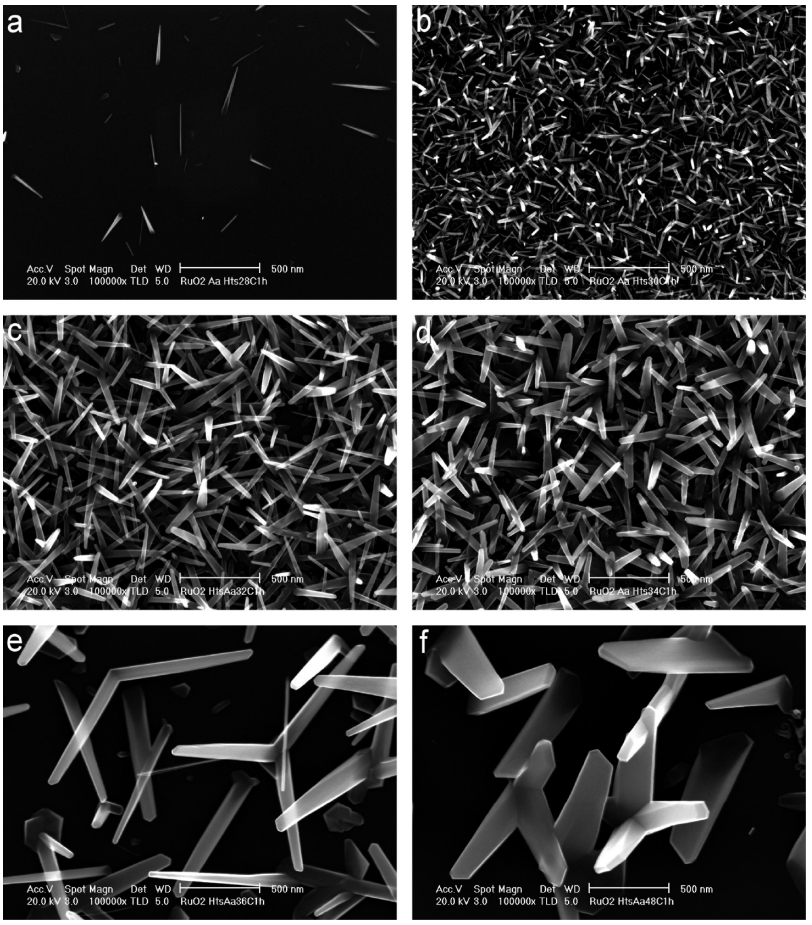

Figure 2. RuO_2 NRs converted for 1 h at different temperatures: (a) 280 °C, (b) 300 °C, (c) 320 °C, (d) 340 °C, (e) 360 °C, and (f) 480 °C.

Table 1. Dimensions of RuO_2 NRs Converted at Different Temperatures

temperature (°C)	average diameter (nm)	average length (nm)	aspect ratio
280	28.9 (±5.6)	347 (±44)	12.5
300	16.5 (±2.2)	118 (±15)	7.3
320	46.3 (±6.1)	499 (±39)	10.8
340	64.6 (±8.3)	581 (±47)	9.0
360	110 (±20.3)	869 (±88)	8.1
480	215 (±58.2)	794 (±115)	3.9

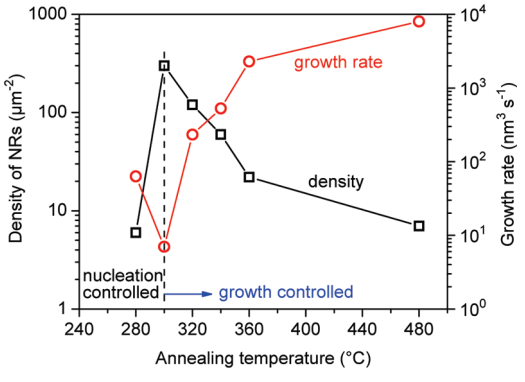

Figure 3. Number density and average growth rate of RuO_2 NRs versus the temperature of heat treatment, showing two synthesis regimes: nucleation controlled and growth controlled.

substrate. Index of the peaks indicates that the RuO_2 NRs exhibit rutile structure with a space group of $P4_2/mnm$ (ICDD file No. 73-1469). The crystallography and microstructure of

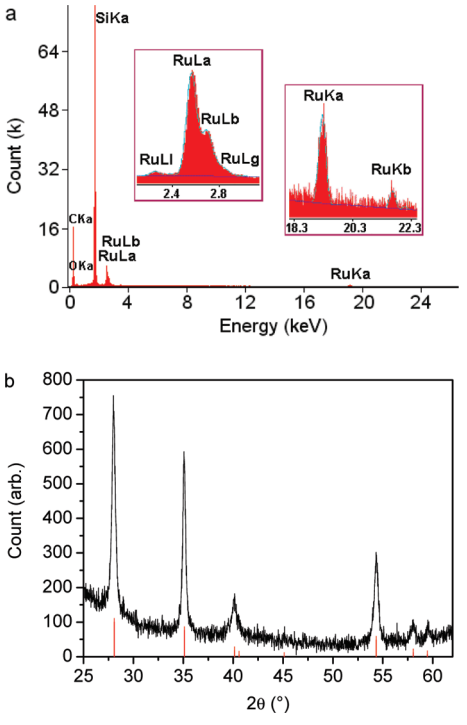

Figure 4. (a) EDS spectrum and (b) XRD pattern of RuO_2 NRs grown at 360 °C, with the red bars indicating the diffraction positions of tetragonal RuO_2 phase (rutile-type) according to ICDD file No. 73-1469.

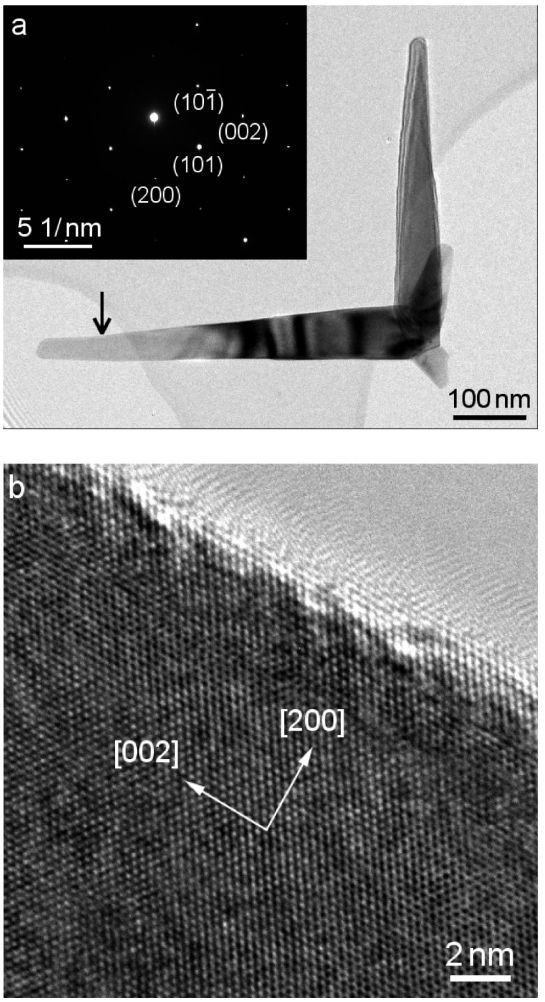

Figure 5. (a) Low magnification TEM micrograph of RuO_2 NRs converted at 320 °C for 1 h and SAED pattern of the horizontal NR in the inset and (b) high resolution TEM micrograph of the edge of the NR marked by an arrow in (a).

the NRs formed were further studied with TEM. Figure 5a shows a typical TEM micrograph of RuO_2 nanorods of obelisk shape. The nanorods have twinned branches grown at right angles from each other, which are commonly observed in the SEM micrographs. The SAED pattern in the inset of Figure 5b reveals their single crystalline nature with [001] orientation along the growth direction. The high-resolution TEM micrograph presented in Figure 5b confirms the growth direction of RuO_2 NRs along the [001] direction with a plane spacing of 1.55 Å, and a lateral [100] orientation with a plane spacing of 2.27 Å. This observation supports the result of XRD analysis.

The anisotropic growth of the NRs can be explained as the minimization of the surface energy of different facets. According to first-principles calculations of rutile TiO_2 stoichiometric surfaces,[15] the surface energy of differently oriented surfaces (facets) follows the sequence: (110) < (100) < (011) < (001). A three-dimensional plot of the equilibrium shape of rutile TiO_2 crystal was further proposed, based on the Wulff construction.[16] It can be tacitly assumed that qualitatively the surfaces of rutile RuO_2 exhibit behavior similar to TiO_2; that is, the {110} planes have the lowest surface energy and the growth direction follows the ⟨001⟩ direction. Indeed, this is confirmed in our HR-TEM images.

It is important to emphasize that our method points to a general synthesis route for 1D oxide nanomaterials. In Figure 6 it

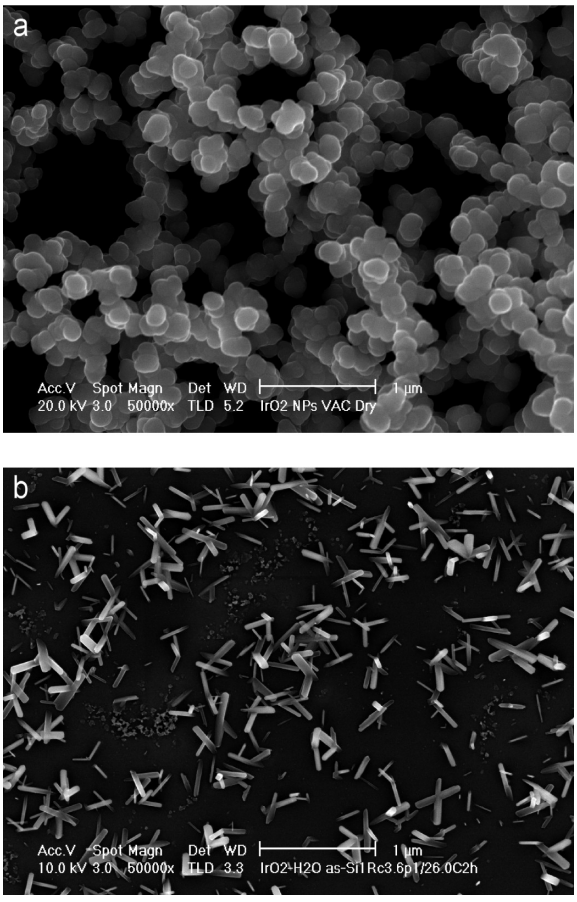

Figure 6. (a) As-prepared $IrO_2 \cdot xH_2O$ NPs precursor film and (b) IrO_2 NRs converted at 600 °C for 2 h.

is also shown that IrO_2 nanorods have been successfully converted from amorphous $IrO_2 \cdot xH_2O$ nanoparticles precursor via the same procedure as described for RuO_2 nanorods. The major difference is that the thermal conversion must be done at higher temperatures, for example, 600 °C for 2 h, due to higher crystallization temperature of the oxide. HR-TEM images revealed unambiguously that the growth of IrO_2 nanorods occurs also along the ⟨001⟩ direction. The facets of IrO_2 nanorods are even more clear than that of RuO_2, confirming the assumption of the Wulff construction controlling the morphology.

NRs are in particular interesting in field emission applications, and therefore the field emission of RuO_2 NRs was conducted in a vacuum of 10^{-4} Pa pressure, with a tungsten tip as the counterpart electrode. In order to improve the conductivity of the silicon substrate, Ti thin film of optimized thickness (100 nm thick) was deposited by magnetron sputtering before thermal conversion. The specimen was heat-treated at 320 °C for 1 h. The RuO_2 NRs grown on Ti/Si(100) substrate have an average length about 200 nm and density around 100 μm^{-2}, which is slightly shorter and thinner than those formed on Si substrate as shown in Figure 7a. The emission current density versus electric field curve of RuO_2 NRs exhibits the Fowler−Nordheim (F−N) behavior,[17] as shown in Figure 7b. Accordingly, the current density can be expressed as

$$J = A\left(\frac{\beta^2 E^2}{\phi}\right) \exp\left(-\frac{B\phi^{3/2}}{\beta E}\right) \quad (1)$$

where J is the current density, constants $A = 1.54 \times 10^{-6}$ A V^{-2} eV and $B = 6.83 \times 10^3$ V $eV^{-3/2}$ μm^{-1}, β is the field enhancement

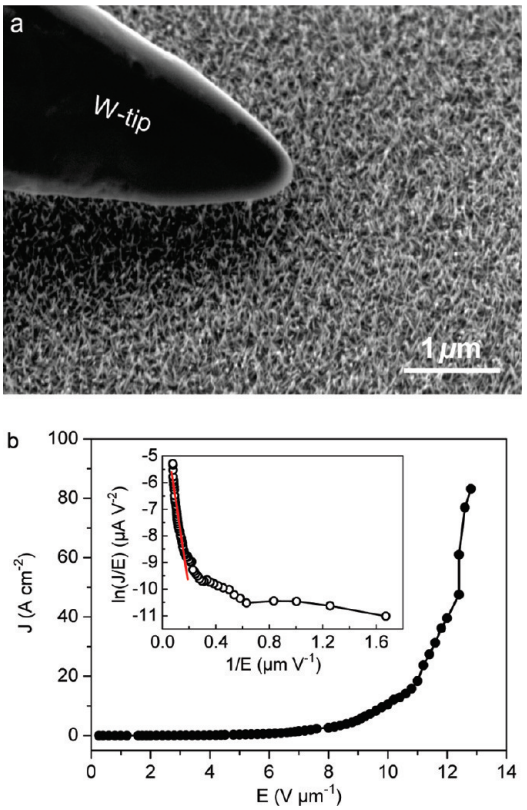

Figure 7. (a) SEM micrograph of field emission test with the specimen tilted 55°. To give a direct measure of the field emission distance between the tungsten tip and RuO_2 NRs, the micrograph is stretched along the vertical direction for correction of the stage tilt; (b) typical field emission $J-E$ curve of RuO_2 NRs. The inset shows the Fowler−Nordheim plot ($\ln(J/E)$ versus $1/E$), which exhibits a linear dependence as indicated.

factor, E is the electric field (V μm^{-1}) defined as $E = V/d$ (d is the field emission distance), and ϕ is the work function that is 4.87 eV for RuO_2.[18] By plotting $\ln(J/E^2)$ as a function of $1/E$, a linear relationship known as a F−N plot is obtained (see the inset in Figure 7b). Then the factor β can be deduced from the line slope S:

$$\beta = -\frac{B\phi^{3/2}}{S} \quad (2)$$

The β is found 2200 for the tested specimen, which is comparable to the best results of carbon nanotubes, ZnO nanowire, or other 1D structures.[12,19−21] The turn-on field E_{to} and threshold field E_{thr} have been proposed as the macroscopic field E needed to produce a current of 10 $\mu A\ cm^{-2}$ and 10 mA cm^{-2}, respectively.[22] The synthesized RuO_2 NRs exhibited a very low turn-on field of less than 0.26 V μm^{-1}, which was the smallest detectable ramping step technically limited by the experimental setup employed. The threshold field was also as low as 1.73 V μm^{-1} and the maximum emission current density of 83A cm^{-2} was obtained at a field of 12.8 V μm^{-1}, which indicates that the RuO_2 NRs could be used as an excellent candidate for a low-operation field and high-brightness electron source.

The field enhancement factor (β) is closely related to the emitter geometry, crystalline structure, and spatial distribution of the emitting centers. It has demonstrated that the field emission performance of ZnO nanowires/nanobelts can be significantly enhanced by increasing the field enhancement factor via either changing the geometrical configuration, decreasing the area density of the nanowires, or increasing the nanowire/nanobelt aspect ratio.[23] The synthesized RuO_2 nanorods of obelisk shape have a nanometric thin diameter, high aspect ratio, and especially atomic sharp pyramid tip, which may exhibit an extreme confinement effect and give a high field enhancement factor. The improvement of field emission performance with decreasing nanorods/nanowires density is attributed to the reduction of a screening effect. For carbon nanotubes (CNTs), an optimum spacing to length ratio of 2:1, 1:1, and 1:2 has been proposed, respectively.[24−26] The tested RuO_2 NRs on Ti/Si(100) substrate have an average length about 200 nm and spacing of 100 nm, and thus a spacing to length ratio of 1:2. The ratio is at the same level as proposed for CNTs, and still yields extreme low turn-on field and threshold field comparable to that of CNTs.[27]

4. Conclusions

Single-crystalline RuO_2 nanorods have been synthesized for the first time by heat-treating amorphous $RuO_2 \cdot xH_2O$ nanoparticle precursors. The shape and size of RuO_2 NRs can be well controlled by varying the heat-treatment conditions. The proposed dissociation−crystallization process may explain the growth mechanism. The well-known Wulff construction rules the anisotropic growth of RuO_2 nanorods. These nanorods exhibit outstanding performance of field emission. Our experiments also show the successful conversion of $IrO_2 \cdot xH_2O$ nanoparticle precursors into IrO_2 nanorods. In conclusion: the approach presented, based on the thermal conversion of amorphous nanoparticle precursors into single crystalline nanorods, points to a generic route for the synthesis of 1D oxide nanomaterials.

Acknowledgment. The authors acknowledge financial support from the Foundation for Fundamental Research on Matter (FOM-Utrecht), the Materials Innovation Institute M2i (www.M2i.nl) in the Netherlands, the former Netherlands Institute for Metals Research, Delft, the Netherlands.

References

(1) Cui, Y.; Wei, Q.; Park, H.; Lieber, C. M. *Science* **2001**, *293*, 1289.
(2) Kolmakov, A.; Klenov, D. O.; Lilach, Y.; Stemmer, S.; Moskovits, M. *Nano Lett.* **2005**, *5*, 667.
(3) Bertoncello, P.; Edgeworth, J. P.; Macpherson, J. V.; Unwin, P. R. *J. Am. Chem. Soc.* **2007**, *129*, 10982.
(4) Xia, Y.; Yang, P.; Sun, Y.; Wu, Y.; Mayers, B.; Gates, B.; Yin, Y.; Kim, F.; Yan, H. *Adv. Mater.* **2003**, *15*, 353.
(5) Hoefelmeyer, J. D.; Niesz, K.; Somorjai, G. A.; Tilley, T. D. *Nano Lett.* **2005**, *5*, 435.
(6) Calarco, R.; Meijers, R. J.; Debnath, R. K.; Stoica, T.; Sutter, E.; Luth, H. *Nano Lett.* **2007**, *7*, 2248.
(7) Tang, Z. Y.; Kotov, N. A.; Giersig, M. *Science* **2002**, *297*, 237.
(8) Tang, Z. Y.; Wang, Y.; Sun, K.; Kotov, N. A. *Adv. Mater.* **2005**, *17*, 358.
(9) Mokari, T.; Rothenberg, E.; Popov, I.; Costi, R.; Banin, U. *Science* **2004**, *304*, 1787.
(10) Chen, Z. G.; Qiu, X. P.; Lu, B.; Zhang, S. C.; Zhu, W. T.; Chen, L. Q. *Electrochem. Commun.* **2005**, *7*, 593.
(11) Ducati, C.; Dawson, D. H.; Saffell, J. R.; Midgley, P. A. *Appl. Phys. Lett.* **2004**, *85*, 5385.
(12) Hsieh, C. S.; Tsai, D. S.; Chen, R. S.; Huang, Y. S. *Appl. Phys. Lett.* **2004**, *85*, 3860.
(13) Korotcov, A.; Hsu, H. P.; Huang, Y. S.; Tsai, D. S.; Tiong, K. K. *Cryst. Growth Des.* **2006**, *6*, 2501.
(14) Herbots, N.; Shaw, J. M.; Hurst, Q. B.; Grams, M. P.; Culbertson, R. J.; Smith, D. J.; Atluri, V.; Zimmerman, P. *Mater. Sci. Eng., B* **2001**, *87*, 303.
(15) Ramamoorthy, M.; Vanderbilt, D. *Phys. Rev. B* **1994**, *49*, 16721.

(16) Wulff, G.; Kristallogr, A. *Mineral* **1901**, *34*, 449.
(17) Fowler, R. H.; Nordheim, L. W. *Proc. R. Soc. A* **1928**, *119* (781), 173.
(18) Tomkiewicz, M.; Huang, Y. S.; Pollak, F. H. *J. Electrochem. Soc.* **1983**, *130*, 1514.
(19) Chen, Z. G.; Zou, J.; Wang, D. W.; Yin, L. C.; Liu, G.; Liu, Q. F.; Sun, C. H.; Yao, X. D.; Li, F.; Yuan, X. L.; Sekiguchi, T.; Lu, G. Q.; Cheng, H. M. *Adv. Funct. Mater.* **2009**, *19*, 484.
(20) Zhang, Q. Y.; Xu, J. Q.; Zhao, Y. M.; Ji, X. H.; Lau, S. P. *Adv. Funct. Mater.* **2009**, *19*, 742.
(21) Gautam, U. K.; Panchakarla, L. S.; Dierre, B.; Fang, X. S.; Bando, Y.; Sekiguchi, T.; Govindaraj, A.; Golberg, D.; Rao, C. N. R. *Adv. Funct. Mater.* **2009**, *19*, 131.
(22) Bonard, J. M.; Salvetat, J. P.; Stockli, T.; De Heer, W. A.; Forro, L.; Chatelain, A. *Appl. Phys. Lett.* **1998**, *73*, 918.
(23) Wang, W. Z.; Zeng, B. Q.; Yang, J.; Poudel, B.; Huang, J. Y.; Naughton, M. J.; Ren, Z. F. *Adv. Mater.* **2006**, *18*, 3275.
(24) Nilsson, L.; Groening, O.; Emmenegger, C.; Kuettel, O.; Schaller, E.; Schlapbach, L.; Kind, H.; Bonard, J. M.; Kern, K. *Appl. Phys. Lett.* **2000**, *76*, 2071.
(25) Suh, J. S.; Jeong, K. S.; Lee, J. S.; Han, I. T. *Appl. Phys. Lett.* **2002**, *80*, 2392.
(26) Bocharov, G. S.; Eletskii, A. V. *Tech. Phys.* **2005**, *50*, 944.
(27) Rao, A. M.; Jacques, D.; Haddon, R. C.; Zhu, W.; Bower, C.; Jin, S. *Appl. Phys. Lett.* **2000**, *76*, 3813.